I&EC research
Industrial & Engineering Chemistry Research
Article
Cite This: Ind. Eng. Chem. Res. XXXX, XXX, XXX−XXX
pubs.acs.org/IECR

Effects of Impurities on CO_2 Sequestration in Saline Aquifers: Perspective of Interfacial Tension and Wettability

Cong Chen,*[†] Zhuang Chai,[†] Weijun Shen,[‡] and Weizhong Li[†]

[†]Key Laboratory of Ocean Energy Utilization and Energy Conservation of Ministry of Education, Dalian University of Technology, Dalian 116024, P. R. China

[‡]Key Laboratory for Mechanics in Fluid Solid Coupling Systems, Institute of Mechanics, Chinese Academy of Sciences, Beijing100190, P. R. China

Supporting Information

ABSTRACT: In recent years, the reduction of CO_2 emissions has become a joint effort throughout the world, and carbon capture and sequestration (CCS) is an effective approach to solving the problem of CO_2 emissions. In the present study, the effects of adding CH_4, Ar, and H_2S to CO_2 on the interfacial tension (IFT) and wettability (contact angle, CA) of the CO_2/water/silica system have been investigated using molecular dynamics simulation methods at 20 MPa and 318 K when the molar concentration of impurity gas was fixed at 20%. For the conditions studied, (1) CH_4 has no significant effect; (2) Ar leads to a higher IFT, a larger CA on silica surfaces with a high hydroxyl density, and a smaller CA on silica surfaces with a low hydroxyl density; and (3) H_2S causes a decrease of the IFT and an increase of the CA. Capillary pressure and gas storage capacity were predicted using IFT and CA data, and the variation of IFT and CA were explained based on density profiles normal to the gas/water and gas/silica interfaces. These findings might be helpful for better understanding the effects of impurities on CCS.

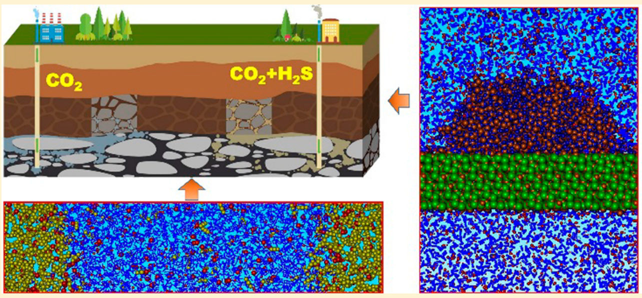

1. INTRODUCTION

In recent years, with the increase in CO_2 emissions, the climate has changed. Issues such as global warming and the greenhouse effect have drawn worldwide attention. CO_2 capture and storage (CCS) technology is the primary choice for countries to tackle carbon emissions.[1,2] CCS is a technology for CO_2 capture and storage that involves collecting CO_2 produced from life and production and storing it in a geological structure.[3] The depth of CO_2 burial is generally more than 800 m, to achieve the supercritical state of CO_2 ($T > 31.1$ °C, $P > 7.38$ MPa). The geological structures used for CCS generally include abandoned oil fields, unworkable gas fields, saline aquifers, and infertile coal mines.[4−10] At the same time, scientists use the collected CO_2 to displace reservoir oil and drive gas (natural gas, coalbed methane), improving the efficiency of mining.[11−15]

The flow and distribution of CO_2 in an enclosed geological structure are very complicated. The interfacial characteristics (interfacial tension, wettability) play an important role in the migration of CO_2, its capture capacity, CO_2 leakage, and storage capacity estimates.[16−18]

In two-phase flow, fluid is divided into wetting and nonwetting phases according to the contact angle. For processes involving CO_2 and water in geological formations, generally, water is considered to be the wetting phase, and CO_2 is considered to be the nonwetting phase.[19] The process by which the nonwetting phase displaces the wetting phase gradually reduces the wetting-phase saturation and is called the drainage process. In contrast, the process by which the wetting phase displaces the nonwetting phase results in a gradual increase in the wetting-phase saturation and is called the moisture process. Capillary pressure is an important characteristic parameter describing the two-phase displacement process in porous media, and it is given by the equation

$$P_C = P_g - P_w = \frac{2\Upsilon_{wg}\cos(\theta)}{R} \tag{1}$$

where P_C is the capillary pressure, P_g is the gas pressure, P_w is the water pressure, Υ_{wg} is the interfacial tension (IFT) between water and gas, θ is the contact angle (CA), and R is the radius of the capillary hole.

The main mechanisms of CO_2 capture in geological structures are structure capture, residual capture, dissolution capture, and mineralization capture.[18] Interfacial tension and wettability have significant effects on residual trapping. In the path of CO_2, when water flows into a region that has been occupied by CO_2 (the water absorption process), part of the CO_2 is adsorbed on the surface of the ore particles because of

Received: September 19, 2017
Revised: December 14, 2017
Accepted: December 18, 2017
Published: December 18, 2017

DOI: 10.1021/acs.iecr.7b03873
Ind. Eng. Chem. Res. XXXX, XXX, XXX−XXX

the capillary force of the sand in the sandstone and remains in the pores.[18]

Ensuring safety and long-term stability and preventing CO_2 leakage are key points in CCS. The main pathways of CO_2 leakage are caprocks, faults, cracks, and abandoned wells.[19−21] Interfacial tension and wettability mainly affect caprock leakage. When capillary pressure reaches or exceeds a threshold, part of the CO_2 leaks through the caprock to the upper strata. Interfacial tension and contact angle also affect the CO_2 storage capacity. Indeed, CO_2 storage capacity can be estimated as[22]

$$M = \frac{2\Upsilon_{wg}\rho_g\Phi(1 - S_w)\cos(\theta)}{(\rho_w - \rho_g)gR} \tag{2}$$

where M is the stored CO_2 mass per unit surface area in saline aquifers, ρ_g is the density of gas, ρ_w is the density of water, S_w is the residual saturation of water, Φ is the porosity, and g is the constant of gravitational acceleration.

Aside from CO_2, there are many other gases in exhaust gas from production and everyday life, such as CH_4, Ar, and H_2S. Conventional storage technology captures CO_2 before storage, which no doubt greatly increases the cost of CO_2 geological storage. Therefore, an effective means of improving the efficiency of CO_2 geological storage would be storing the exhaust gas directly.[23] To better understand the migration process of CO_2 gas mixtures, the effects of impurities on interfacial tension and wettability must be fully investigated.

Khosharay and Varaminian simulated $(N_2 + CO_2) + H_2O$ at different temperatures and pressures and successfully determined that the contents of CO_2, N_2, and H_2O are key parameters influencing the interfacial tension.[24] Chow et al. conducted experiments that measured the interfacial tension of $(N_2 + CO_2) + H_2O$ at different temperatures (298−488 K) and pressures (0−50 MPa).[25] Saraji et al. concluded that the interfacial tension between $(CO_2 + SO_2)$ and brine decreased linearly with increasing amount of SO_2 in the CO_2-rich phase.[26] Later, Chow et al.[27] conducted other experiments that measured the interfacial tension of $(Ar + CO_2) + H_2O$ using the hanging drop method and found that the statistical associating fluid theory for variable range potentials of the Mie form (SAFT-VR Mie) provides an excellent description of the interfacial tension of water and a correlation of the interfacial tension in the binary system.[27] Ren et al. measured the interfacial tensions of $(CO_2 + CH_4)$ + water systems with five gas compositions and found that, under fixed temperature and pressure conditions, the interfacial tensions of all five gas mixtures decreased as the mole fraction of CO_2 was increased. The change was not linear, with larger changes observed in the range of higher CO_2 mole concentrations.[28] Liu et al.[29] employed the axisymmetric drop shape analysis (ADSA) method to measure the interfacial tension between $(CO_2 + CH_4)$ and brine over the temperature range from 77.0 to 257.0 °F and the pressure range from 15 to 5027 psia. Their test results showed that the presence of CO_2 decreased the interfacial tension of CH_4/H_2O or CH_4/brine (NaCl) systems, with the degree of reduction depending on the molar fraction of CO_2 in the gas mixture.[29] Shah et al.[30] first performed interfacial tension measurements for water/H_2S systems over a large range of pressures (up to $P = 15$ MPa) and temperature (up to $T = 120$ °C) by the hanging drop technique under geological storage conditions. They observed that the interfacial tension between water and $(CO_2 + H_2S)$ at $T = 77$ °C and $P > 7.5$ MPa was approximately equal to the molar average interfacial tension of the water/CO_2 and water/H_2S binary mixtures. Thus, when the H_2S content in the stored acid gas was increased, the capillary entry pressure decreased, together with the maximum height of the acid gas column and the potential storage capacity of a given geological formation.[30]

Using molecular dynamics simulations, Al-Yaseri et al. conducted interfacial tension and contact angle measurements under the Gippsland basin storage conditions (13 MPa, 333 K). They found that CO_2 had a relatively higher water contact angle ($\theta = 47°$), whereas lower θ values were measured for N_2 ($\theta = 40.6°$) and for 50 mol % CO_2 + 50 mol % N_2 ($\theta = 33.9°$).[31] Saraji et al. reported that rock wettability was not affected by SO_2.[26] To take into account the mixed-gas nature (CO_2, CH_4, and a lesser extent of N_2) of the coal seam gas in the Sydney Basin in Australia, Saghafi et al. evaluated the relative wettabilities of coal by CH_4, CO_2, and N_2 gases in the presence of water.[32] Bagherzadeh et al.[33] studied the hydrated silica−water interface in the presence of methane or carbon dioxide gas with molecular dynamics simulations. They found that the water number density in the layers adjacent to the silica was higher and that these layers were more structured and less mobile compared with water layers far from the surface. McCaughan et al.[34] simulated the contact angle of the CO_2/water/quartz system and separately added N_2 and H_2S to the CO_2. They found that, when N_2 was added to the simulation system, the contact angle of water on the quartz surface was reduced because of the special properties of N_2, that is, the wettability of water on the quartz surface was increased. In contrast, when H_2S was added to the simulation system, the contact angle of water on the quartz surface increased, that is, the wettability of water on the quartz surface was reduced.[34]

For CH_4, there have been several experimental and simulation studies on interfacial tension.[28,29] To the best of our knowledge, the effects of CH_4 and Ar on wettability specifically for CCS are open to question. For H_2S, Shah et al.[30] performed experiments to explore the effects on interfacial tension, and McCaughan et al.[34] simulated the contact angle of the $(H_2S + CO_2)$/water/quartz system. However, they did not consider the effects of hydroxyl functional group on the quartz surface. In the present study, the influences of adding CH_4, Ar, and H_2S to CO_2 on the interfacial tension and wettability of the CO_2/water/silica system were investigated. At the same time, because of the significant effects on wettability of functional groups on the silica surface, in simulations of the contact angle, two silica surfaces with different hydroxyl-group densities were employed.[35]

2. METHODS

2.1. Interfacial Tension Model. One cubic water box and two cubic gas-mixture boxes were constructed with the same length of 60 Å. The water box was sandwiched by the two gas-mixture boxes to construct two water/gas interfaces normal to the z direction. Four sets of gas systems were designed, composed of CO_2 and CH_4, CO_2 and H_2S, CO_2 and Ar, and pure CO_2. In the mixtures with other gases, the molar concentrations of CO_2 and the other gas were 80% and 20%, respectively. The configurations of these simulation boxes are illustrated in Figure 1.

2.2. Contact Angle Model. Silyl groups on silica surfaces in which each silicon contains zero, one, and two hydroxyl groups are usually denoted as Q^4, Q^3, and Q^2, respectively.

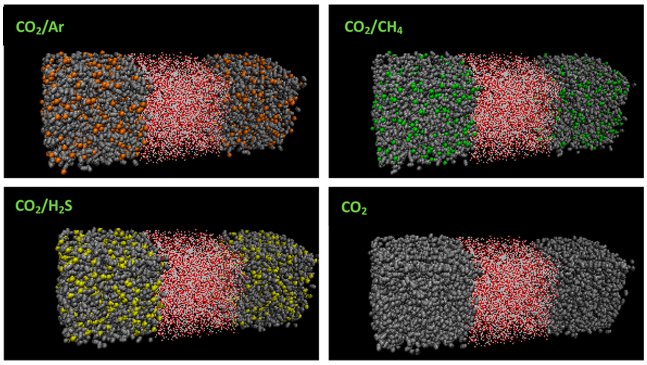

Figure 1. Four interfacial tension models. Gas molecules are presented in vdW format (solid van der Waals spheres for atoms), and water molecules are presented in line format (simple lines for bonds and points for atoms). Ar, orange; CH_4, green; CO_2, silver; H_2S, yellow.

Two (001) silica surfaces were selected, namely, Q^3 and Q^3/Q^4. Q^3/Q^4 is a combination of the Q^3 and Q^4 surfaces with a hydroxyl-group number density of 2.4 OH/nm^2. The hydroxyl-group number density of the Q^3 surface is 4.7 OH/nm^2. Snapshots of these two silica models are shown in Figure 2.

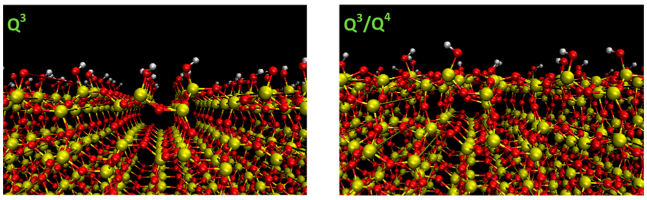

Figure 2. Two silica models: Q^3 and Q^3/Q^4. Silica and hydroxyl are presented in CPK format (atoms as spheres and bonds as cylinders).

The silica surface was placed horizontally. Then a half-cylindrical water droplet was placed onto the surface. The gas mixture was distributed on the upper and lower sides of the silica surface. The dimensions in the x and z directions were long enough to ensure that the room for the motion of the water molecules was sufficiently large. A typical simulation box is illustrated in Figure 3.

2.3. Force Field.

The simulations were based on the CHARMM[36] force-field model. In the CHARMM force field, the nonbonded potential between interaction sites that are separated by more than two bonds or belong to different molecules is described by the Lennard-Jones (LJ) 12−6 potential

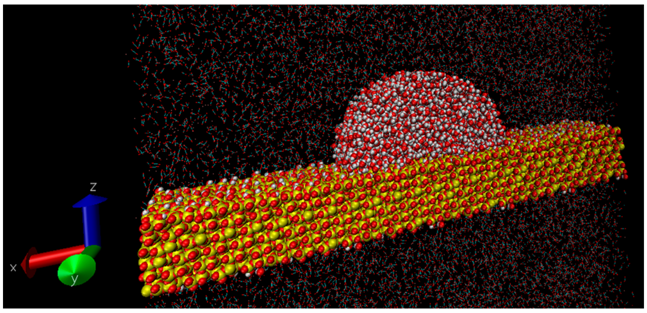

Figure 3. Snapshot of the simulation box for predicting the water contact angle. Silica and water are presented in vdW format (solid van der Waals spheres for atoms), and CO_2 mixture molecules are presented in line format (simple lines for bonds and points for atoms).

$$U(r_{ij}) = 4\varepsilon_{ij}\left[\left(\frac{\sigma_{ij}}{r_{ij}}\right)^{12} - \left(\frac{\sigma_{ij}}{r_{ij}}\right)^{6}\right] \tag{3}$$

where r_{ij}, ε_{ij}, and σ_{ij} are the separation, LJ well depth, and LJ size, respectively, for the pair of atoms i and j. The LJ parameters are listed in Table 1. Unlike interactions were computed using standard Lorentz−Berthelot combining rules

$$\sigma_{ij} = \frac{1}{2}(\sigma_i + \sigma_j) \tag{4}$$

$$\varepsilon_{ij} = \sqrt{\varepsilon_i \varepsilon_j} \tag{5}$$

Table 1. Parameters of the Lennard-Jones Potential and Charges

pseudoatom	ε (kcal·mol^{-1})	σ (Å)	q (e)	ref
C (in CO_2)	0.056	2.76	0.6512	37
O (in CO_2)	0.160	3.03	−0.3256	37
CH_4	0.294	3.73	0	38
Ar	0.240	3.41	0	39
H (in H_2S)	0.008	0.98	0.124	40
S (in H_2S)	0.497	3.72	−0.248	40
H (in H_2O)	0	0.0001	0.4238	41
O (in H_2O)	0.155	3.17	−0.8476	41

The bond-stretching potential is given by

$$U_b = K_b(b - b_0)^2 \tag{6}$$

where K_b, b, and b_0 are the spring constant, the distance between atoms, and the equilibrium distance, respectively.[42]

The bond-bending potential is given by

$$U_\theta = K_\theta(\theta - \theta_0)^2 \tag{7}$$

where K_θ, θ, and θ_0 are the angle constant, the angle in radians between two bonds, and the equilibrium angle in radians, respectively.[42]

The parameters of the bond-stretching potential and the bond-bending potential are provided in Table 2.

Only parameters for gas and water are listed in Tables 1 and 2. For silica, the force-field parameters were derived from ref 41. This silica force field was selected because it was originally introduced to reduce uncertainties in computed interfacial properties such as interfacial tension and contact angles. The details of the silica force-field parameters are summarized in the Supporting Information.

2.4. Simulation Details.

All of the simulations were conducted using the NAMD program, an open-source molecular dynamics simulation package.[43] Periodic boundary conditions were applied in three dimensions. For the nonbonded force-field parameters, a switching function and neighborhood lists were used. To improve energy conservation, a smooth switching function was used to truncate the van der Waals potential energy smoothly at the cutoff distance. The cutoff distance was 13.5 Å, and the switching process was started at 12.0 Å. Neighborhood lists were updated every 10 time steps. The particle mesh Ewald (PME) method[44] was used for electrostatics.

DOI: 10.1021/acs.iecr.7b03873
Ind. Eng. Chem. Res. XXXX, XXX, XXX−XXX

Table 2. Parameters of the Bond-Stretching and Bond-Bending Potentials

bond	b_0 (Å)	K_b (kcal·mol^{-1}·Å^{-2})	angle	θ_0 (deg)	K_θ (kcal·mol^{-1}·rad^{-2})	ref
O−C	1.149	1282.46	O−C−O	180.0	147.60	37
H−O	0.96	540.63	H−O−H	104.5	50.00	41
H−S	1.365	95.84	H−S−H	91.5	62.07	40

The time step was 1 fs. The initial temperature value for the system was 318 K. The time step between calculations of nonbonded interactions was 1 fs, whereas the time step between calculations of the full electrostatic evaluations was 2 fs. The multiple-time-step integration technique reversible reference system propagation algorithm (r-RESPA)[45] was employed.

All simulations were performed in the *NPT* or *NVT* ensemble. In *NPT* simulations, the Langevin piston Nosé−Hoover method, a combination of the Nosé−Hoover constant-pressure method[46] with piston fluctuation control implemented using Langevin dynamics, was applied to fix the system pressure (20 MPa) and temperature (318 K). The piston period and piston decay were 100 time steps and 50 time steps, respectively. The damping coefficient was 5/ps. To release interfacial stress generated during construction, an *NVT* simulation was usually run for 2−3 ns before the *NPT* simulations. Then, additional 15-ns runs were performed, including the first 12-ns run to equilibrate the system and the last 3 ns to obtain output data.

Interfacial tensions were calculated from the pressure tensors recorded in the simulated log file. The pressure parameters in all directions are denoted as P_{xx}, P_{xy}, P_{xz}, P_{yx}, P_{yy}, P_{yz}, P_{zx}, P_{zy}, and P_{zz}. The values of P_{xx}, P_{yy}, and P_{zz} and the size h_z in the z direction were used in the following equation to obtain the interfacial tensions

$$\gamma = \frac{1}{2}h_z\left[P_{zz} - \frac{1}{2}(P_{xx} + P_{yy})\right] \tag{8}$$

During the last 3 ns, pressure-tensor data were recorded every 1 ps, and a total of 3000 groups were generated. Three hundred groups generated an interfacial tension, and finally, a total of 10 interfacial tension data points were used to calculate the average and error values in each simulation box.

Contact angles were predicted from two-dimensional density profiles of water. The density profiles were calculated every 1 ns during the last 3 ns of each simulation. As a result, for each simulation, six contact-angle data points were available for the calculation of the average and error values. All data were processed using the molecular graphics software Visual Molecular Dynamics (VMD)[47] with in-house codes.

3. RESULTS AND DISCUSSION

3.1. Validity. Under the experimental conditions, the interfacial tensions between gas and water were predicted, and the results were compared with experimental values to verify the accuracy of the force-field parameters. The experimental and simulated results are reported in Table 3 (pure CO_2 was validated in a previous article[48]). The good agreement between the simulated and experimental data demonstrates the accuracy of the force-field parameters.

3.2. Interfacial Tension. Molecular dynamics simulations were performed, and the final configurations for the CO_2/Ar, CO_2/CH_4, CO_2/H_2S, and pure CO_2 systems are illustrated in Figure 4.

Table 3. Experimental and Simulated Interfacial Tensions between Gas and Water (mN/m)

gas	T (K)	P (MPa)	experiment	simulation
CO_2/Ar[a]	297.94	20	31.10 ± 0.56[27]	39.23 ± 3.01
CO_2/CH_4[b]	298.15	10	38.65 ± 0.06[28]	41.20 ± 1.62
CO_2/H_2S[c]	350.15	10	29.20 ± 0.30[30]	20.95 ± 0.46

[a] 50.27 mol % Ar + 49.76 mol % CO_2. [b] 80 mol % CO_2 + 20 mol % CH_4. [c] 70 mol % CO_2 + 30 mol % H_2S.

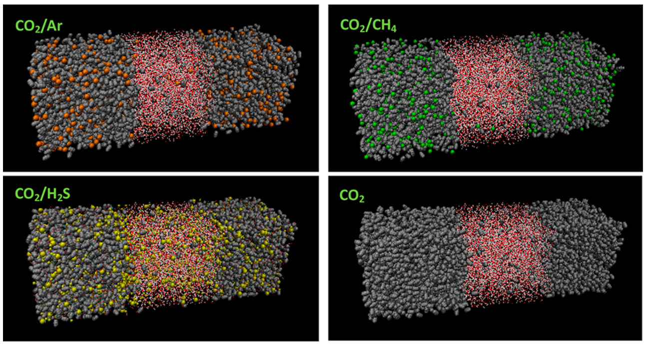

Figure 4. Four groups of interfacial tension models after simulation. CO_2 and other gases are presented in vdW format, and water molecules are presented in line format. Ar, orange; CH_4, green; CO_2, silver; H_2S, yellow.

The distributions of the gas mixtures in different groups are different (Figure 4). In the interfacial tension model of CO_2/H_2S, water dissolves a great deal of H_2S, and the distribution of H_2S is very uniform. This is related to H_2S ionization in water.[49] The results for the interfacial tensions are reported in Table 4.

Table 4. Predicted Interfacial Tensions for Different Gas Mixtures with Water

gas	X_{CO_2}	average (mN/m)	error (mN/m)
CO_2 + Ar	0.8	34.10	0.96
CO_2 + CH_4	0.8	32.76	1.49
CO_2 + H_2S	0.8	10.99	1.93
pure CO_2	1.0	31.67	1.51

It is clear that differences in the molecular species lead to differences in the interfacial tensions among the various groups. The different behaviors of the interfacial tensions predicted in this study agree well with those found in the literature. With 20 mol % Ar, the interfacial tension is 34.1 mN/m, whereas that of pure CO_2 and water is 31.67 mN/m, which indicates that the presence of Ar makes the interfacial tension between CO_2 and H_2O larger. In a previous study,[27] the ratio of CO_2 to Ar was 1:1, and when the temperature and pressure were 323 K and 20 MPa, respectively, the interfacial tension between (CO_2 + Ar) and H_2O was found to be 35.5 mN/m. Under the same conditions, the interfacial tension between Ar and H_2O was found to be 59.4 mN/m.

The addition of CH_4 increases the interfacial tension, resulting in a difference of 1.09 mN/m. Liu et al.[29] considered that the presence of CO_2 in CH_4 leads to a reduction in the interfacial tension between gas mixtures and brine. With more CO_2 present in the gas mixture, the effect of the interfacial tension reduction was found to be more pronounced. In other words, the presence of CH_4 in CO_2 increases the interfacial tension between the gas mixtures and brine. Ren et al.[28] reached the same conclusion.

The interfacial tension of the $(CO_2 + H_2S)$/water system is 10.99 mN/m, whereas the interfacial tension of the pure CO_2/water system is 31.67 mN/m. The interfacial tension of the $(CO_2 + H_2S)$/water system is thus about one-third that of the pure CO_2/water system. The presence of H_2S causes the gas/water interfacial tension to drop significantly. In the study of Shah et al.,[30] the authors found that, when the H_2S content in the stored acid gas increased, the capillary entry pressure decreased, along with the maximum height of the acid gas column.

3.3. Contact Angle. The configurations after the end of the simulations for the two different surface structures of silica are shown in Figures 5 and 6. The predicted water contact angles are summarized in Table 5.

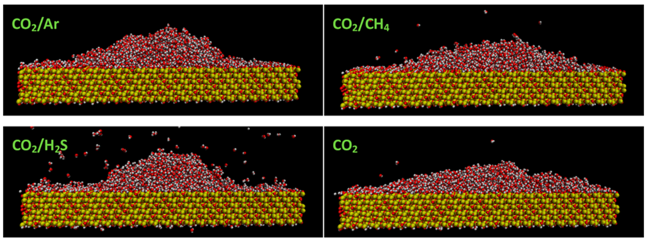

Figure 5. Snapshots of the gas/water/silica system where the surface structure of silica is Q^3.

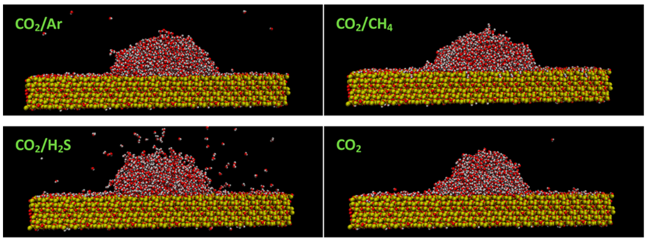

Figure 6. Snapshots of the gas/water/silica system where the surface structure of silica is Q^3/ Q^4.

Table 5. Predicted Water Contact Angles

		Q^3		Q^3/Q^4	
gas	X_{CO_2}	average (deg)	error (deg)	average (deg)	error (deg)
CO_2/Ar	0.8	28.54	2.92	47.76	6.67
CO_2/CH_4	0.8	25.98	3.72	53.15	6.04
CO_2/H_2S	0.8	34.99	5.35	61.89	5.25
pure CO_2	1.0	24.00	4.00	54.23	4.19

When the surface structure of silica is Q^3, the water contact angles for the three gas mixtures CO_2/Ar, CO_2/CH_4, and CO_2/H_2S increase by 4.54°, 1.98°, and 10.99°, respectively, compared with that of pure CO_2. Considering the estimated errors, the effects of Ar and CH_4 can be neglected. A dependence of the water contact angle on the H_2S concentration was also found by McCaughan et al.[34] On the Q^3/Q^4 silica surface, similar results are obtained. However, the increase in the water contact angle for CO_2/H_2S is 7.66°. Water contact angles are strongly related to the hydroxyl-group number density. As the hydroxyl-group number density decreases, the water contact angle increases.[35] The hydroxyl-group number density also seems to affect the increment of the water contact angle for the CO_2/H_2S gas mixture. On the Q^3 surface, which has a hydroxyl-group number density of 4.7 OH/nm^2, when 20 mol % H_2S is added, the water contact angle increases by 45.8%. On the Q^3/Q^4 surface, which has a hydroxyl-group number density of 2.4 OH/nm^2, the water contact angle increases by only 14%.

3.4. Interfacial Structure. To gain further insight into the different adsorption behaviors of CO_2, Ar, CH_4, and H_2S, we calculated the densities of all of these gases in the interfacial tension (IFT) and contact angle (CA) models. These values enable a comparison of the relative wettabilities of Ar, CH_4, H_2S, and CO_2 on the silica surface through an analysis of the fluid density of each molecular fluid as a function of the distance to the silica surface.

3.4.1. Interfacial Tension. In the IFT model, the densities are calculated in the x direction, giving the results shown in Figures 7−9.

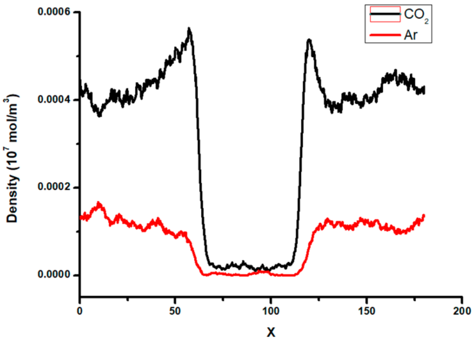

Figure 7. Densities of CO_2 and Ar in the x direction.

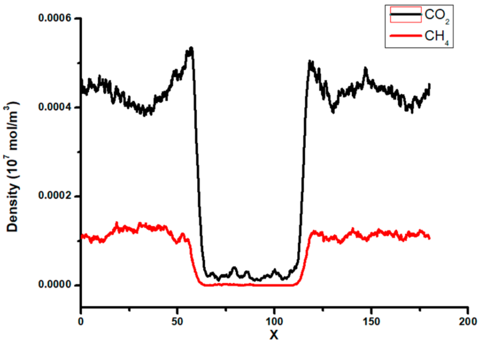

Figure 8. Densities of CO_2 and CH_4 in the x direction.

The middle of the IFT model is water. It can be clearly seen that the hydrophilicities of CH_4 and Ar are not much different from that of CO_2 whereas H_2S exhibits significant hydrophilicity. The densities of CH_4 and Ar do not change significantly when they are near the surface of water, and the CO_2 density increases significantly in $(CO_2 + CH_4)$ and $(CO_2 + Ar)$. In $(CO_2 + H_2S)$, the density of H_2S increases greatly at the surface of water, whereas the change in the CO_2 density is smaller compared with those in $(CO_2 + CH_4)$ and $(CO_2 + Ar)$.

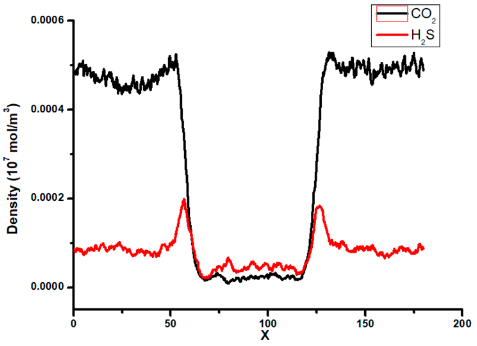

Figure 9. Densities of CO_2 and H_2S in the *x* direction.

These findings confirm that the adsorption capacity of H_2S on the water surface is stronger than those of CH_4 and Ar, so the interfacial tension of (CO_2 + H_2S) is obviously smaller than those of the other two groups.

3.4.2. Contact Angle: Q^3. Because the molar fraction of CO_2 in the simulations was 80% and those of the other gases were 20%, the densities of the remaining gases were multiplied by a factor of 4 for better comparisons. The densities calculated in the *z* direction are shown in Figures 10−12.

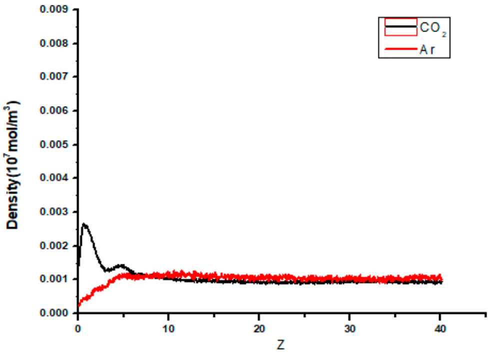

Figure 10. Densities of CO_2 and Ar in the *z* direction.

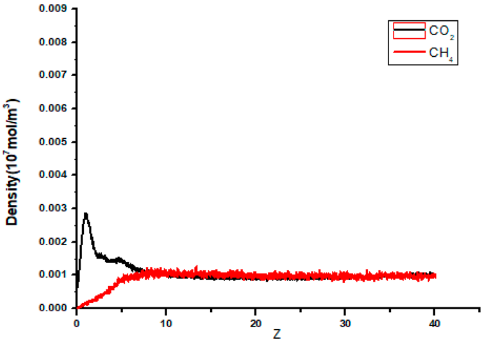

Figure 11. Densities of CO_2 and CH_4 in the *z* direction.

As can be seen, the densities of Ar and CH_4 near the silica surface are very low and even lower than the bulk values. However, the densities of CO_2 and H_2S show peaks near the silica surface. The peak value for H_2S is about 4 times larger than that for CO_2. It can be concluded that H_2S has a higher affinity than the other gases and that the affinities of Ar and CH_4 are less than that of CO_2.

3.4.3. Contact Angle: Q^3/Q^4. The contact angle data for the Q^3/Q^4 surface were handled in the same way as the contact angle data for the Q^3 surface, as described in the preceding section. The densities calculated in the *z* direction are shown in Figures 13−15.

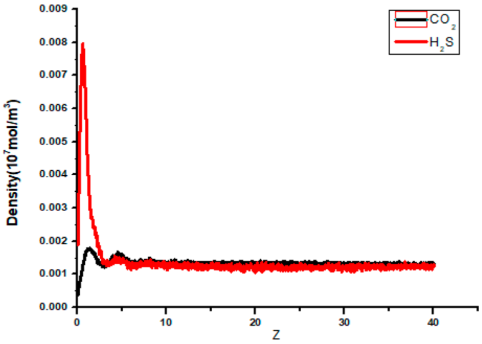

Figure 12. Densities of CO_2 and H_2S in the *z* direction.

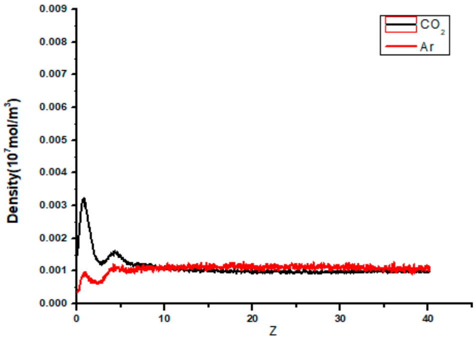

Figure 13. Densities of CO_2 and Ar in the *z* direction.

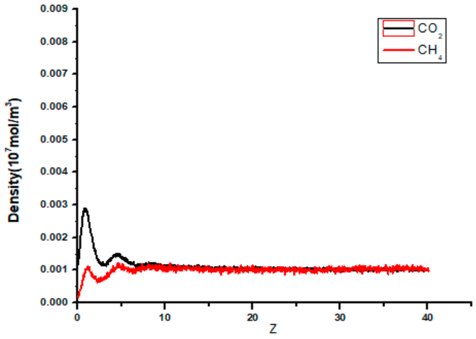

Figure 14. Densities of CO_2 and CH_4 in the *z* direction.

On the Q^3/Q^4 surface, the densities of Ar and CH_4 are again smaller than that of CO_2. However, the trends for Ar and CH_4

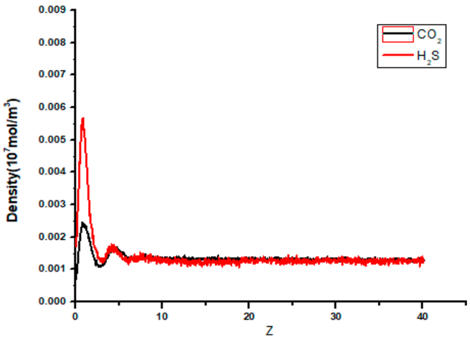

Figure 15. Densities of CO_2 and H_2S in the *z* direction.

become the same as that for CO_2. The peak positions are the same, although the peak values change with gas composition. The number densities of hydroxyl groups on Q^3/Q^4 and Q^3 are 2.4 and 4.7 OH/nm^2, respectively. Ar, CH_4, and CO_2 have higher affinities for the Q^3/Q^4 surface than for the Q^3 surface, whereas H_2S has a lower affinity. This means that the presence of hydroxyl groups results in the degradation of the adsorptions of Ar, CH_4, and CO_2 on silica but the enhancement of the adsorption of H_2S. This explains the smaller relative increment in the water contact angle for CO_2/H_2S on Q^3/Q^4 than for CO_2/H_2S on Q^3.

3.5. Discussion. Interfacial tension and contact angle mainly affect the capillary pressure and CO_2 storage capacity. Assuming that the radius of all of the capillary holes is 40 nm, the simulated values of the interface tension and contact angle were used in eq 1 to obtain the capillary pressures, as reported in Table 6.

Table 6. Capillary Pressures

gas	P_C (MPa) Q^3	 Q^3/Q^4
CO_2/Ar	1.50	1.15
CO_2/CH_4	1.47	0.98
CO_2/H_2S	0.45	0.26
pure CO_2	1.45	0.93

Even though the surface functional groups on the two silica surfaces are of different types, the groups of gases cause the same trend in capillary pressure. For both surfaces, the capillary pressure becomes larger in the order $H_2S < CO_2 < CH_4 < Ar$. Among the four gases, the capillary pressure for H_2S is much smaller than those of the other gases. This means that the coinjection of H_2S increases the risk of gas leakage. To avoid leakage, a given reservoir will sustain a lower gas pressure or a smaller gas column height. For reservoirs composed of minerals with lower hydroxyl-group number densities, the capillary pressure for H_2S is even lower with a higher risk of gas leakage. On the Q^3 surface, the capillary pressures of CO_2, CH_4, and Ar are not much different. Considering data deviations in the simulations, the differences are negligible. However, on the Q^3/Q^4 surface, the capillary pressure of Ar is 0.22 MPa larger than that of CO_2, which implies that the coinjection of Ar with CO_2 is beneficial. The capillary pressure of CH_4 is still close to that of CO_2, showing that mixing a small amount of CH_4 in CO_2 does not have a significant effect on the capillary pressure.

To predict the gas storage capacities of the various systems, we assumed $\Phi = 0.2$, $S_w = 0.1$, $R = 40$ nm, $g = 9.8$ m/s^2, $\rho_w = 998.79$ kg/m^3, and $\rho_g = 813.52$ kg/m^3 and used these values in eq 2. The results are summarized in Table 7.

The storage capacity of CO_2/H_2S is the smallest, whereas the storage capacity of CO_2/Ar is the largest. For a reservoir composed of Q^3 silica, when 20% H_2S is added, the storage capacity decreases by about 70% compared with that of pure CO_2. For Q^3/Q^4, when 20% H_2S is added, the storage capacity drops by about 72%. Thus, coinjection of H_2S with CO_2 is a bad idea, especially for reservoirs composed of minerals with low hydroxyl-group number densities. When 20% Ar is added to pure CO_2, the gas storage capacity increases by 3.5% and 23.8% for Q^3 and Q^3/Q^4 silica reservoirs, respectively. Therefore, coinjection of Ar with CO_2 is beneficial, especially for reservoirs composed of minerals with low hydroxyl-group number densities.

Table 7. Gas Storage Capacities

gas	M ($\times 10^3$ kg/m^2) Q^3	 Q^3/Q^4
CO_2/Ar	120.81	92.44
CO_2/CH_4	118.76	79.23
CO_2/H_2S	36.31	20.88
pure CO_2	116.67	74.65

4. CONCLUSIONS

In the present study, the effects of adding CH_4, Ar, and H_2S to CO_2 on the interfacial tension and wettability of the CO_2/water/silica system were investigated using molecular dynamics simulations at 20 MPa and 318 K. The following results were obtained:

Adding 20% CH_4 to pure CO_2 has no significant effect on the interfacial tension between gas and water. The interfacial tension between Ar/CO_2 and water increases by 7.7% when 20% Ar is mixed with CO_2. However, the presence of H_2S significantly affects the interfacial tension. Adding 20% H_2S causes a 65.3% reduction of the interfacial tension. Further analysis of the density profiles along the gas/water interfaces indicated that the densities of CH_4 and Ar do not change significantly when they are near the surface of water whereas the density of H_2S increases signifcantly at the surface of water. The density profile results confirmed that the adsorption capacity of H_2S on the water surface is stronger than those of CH_4 and Ar, so the interfacial tension of $(CO_2 + H_2S)$ is obviously smaller than those of the other two groups.

Water contact angles for the gas/water systems on Q^3/Q^4 silica are always larger than the values for the gas/water systems with the same gas compositions on Q^3 silica because of the different hydroxyl-group number densities. The composition of the gas mixture affects the water contact angles, and the hydroxyl-group number density also seems to affect the increments of the water contact angles for CO_2/impurity/water−silica systems relative to those of the pure CO_2 systems. The water contact angle for CO_2/water on Q^3 silica increases by 18.9% and 8% when 20% Ar and CH_4, respectively, are added. However, when 20% H_2S is added, the water contact angle rises by 45.8%. On the Q^3/Q^4 silica surface, additions of Ar and CH_4 reduce the water contact angle by about 12% and 2%, respectively, whereas addition of 20% H_2S causes a 14% increase in the water contact angle. The density profiles revealed that the presence of hydroxyl groups causes the degradation of the adsorptions of Ar, CH_4, and CO_2 on silica but the enhancement of the adsorption of H_2S. This explains the lower relative increment in the water contact angle for CO_2/H_2S on Q^3/Q^4 than for CO_2/H_2S on Q^3.

The capillary pressure and gas storage capacity were calculated to further investigate the effects of impurities on CCS. Among the four gases, the capillary pressure for H_2S is much smaller than that of the other gases, leading to a high risk of gas leakage. For reservoirs composed of minerals with lower hydroxyl-group number densities, the capillary pressure of H_2S is even lower. On the Q^3/Q^4 surface, the capillary pressure of Ar is larger than that of CO_2 which implies that the coinjection of Ar with CO_2 is beneficial under some conditions. The storage capacity of CO_2/H_2S is the smallest, whereas the storage capacity of CO_2/Ar is the largest. H_2S impurities should thus be removed, whereas Ar and CH_4 impurities can be retained, especially for reservoirs composed of minerals with low hydroxyl-group number densities.

The composition of impurities generated by industry can change from site to site, so further investigations should be performed for different gas concentrations and mixture types. Two ideal silica structures, namely, Q^3 and Q^3/Q^4, were selected for investigation, whereas the true surface structures of the mineral under reservoir conditions are rather complex and require further studies.

■ ASSOCIATED CONTENT

Supporting Information

The Supporting Information is available free of charge on the ACS Publications website at DOI: 10.1021/acs.iecr.7b03873.

> Illustration of the types of atoms and summary of silica force filed details include the interaction parameters for bond stretching and angle bending, atom partial charges, and LJ parameters (PDF)

■ AUTHOR INFORMATION

Corresponding Author

*E-mail: congchen@dlut.edu.cn. Tel.: 86-411-84708774.

ORCID

Cong Chen: 0000-0001-5035-1026

Notes

The authors declare no competing financial interest.

■ ACKNOWLEDGMENTS

C.C. received funding from National Natural Science Foundation of China (Grants 51676027 and 51206016), the Natural Science Foundation of Liaoning Province (201602147), and the Fundamental Research Funds for the Central Universities (DUT17LAB03).

■ REFERENCES

(1) Benson, S. M.; Surles, T. Carbon dioxide capture and storage: An overview with emphasis on capture and storage in deep geological formations. *Proc. IEEE* **2006**, *94*, 1795−1805.

(2) Kheshgi, H.; de Coninck, H.; Kessels, J. Carbon dioxide capture and storage: Seven years after the IPCC special report. *Mitigation and Adaptation Strategies for Global Change* **2012**, *17*, 563−567.

(3) Lokhorst, A.; Wildenborg, I. Introduction on CO_2 geological storage. Classification of storage options. *Oil Gas Sci. Technol.* **2005**, *60*, 513−515.

(4) Bachu, S. From suitability to ultimate capacity: A roadmap for assessing sedimentary basins and selecting sites for CO_2 storage in geological media. In *Greenhouse Gas Control Technologies: Proceedings of the Fifth International Conference on Greenhouse Gas Control Technologies*; CSIRO Publishing: Collingwood, VIC, Australia, 2001; pp 328−333.

(5) Dyksterhuis, S.; Mueller, R. D. Future intraplate stress and the longevity of carbon storage. *Fuel* **2017**, *200*, 31−36.

(6) Zhang, K.; Cao, L. Analysis of the Possibility of Carbon Dioxide Storage in China's Underground Salt Caverns. *Adv. Mater. Res.* **2014**, *1073−1076*, 2092−2097.

(7) Li, P.; Zhou, D.; Zhang, C.; Chen, G. Assessment of the effective CO_2 storage capacity in the Beibuwan Basin, offshore of southwestern P. R. China. *Int. J. Greenhouse Gas Control* **2015**, *37*, 325−339.

(8) Lutynski, M. A concept of enhanced methane recovery by high pressure CO_2 storage in abandoned coal mine. *Gospod. Surowcami Miner.* **2010**, *26*, 93−104 (in Polish).

(9) Yang, C.; Hovorka, S. D.; Trevino, R. H.; Delgado-Alonso, J. Integrated Framework for Assessing Impacts of CO_2 Leakage on Groundwater Quality and Monitoring-Network Efficiency: Case Study at a CO_2 Enhanced Oil Recovery Site. *Environ. Sci. Technol.* **2015**, *49*, 8887−8898.

(10) Zhang, L.; Ren, S. R.; Zhang, Y.; Yl, P.; Ml, H. G.; Ma, Y. X. Geological Storage of CO_2 in DF1-1 Gas Field South China Sea: Design of a Demonstration Project. Presented at the *Canadian International Petroleum Conference 2009 and 60th Annual Technical Meeting of the Petroleum Society*, Calgary, Alberta, Canada, Jun 16−18, 2009.

(11) Bachu, S.; Shaw, J. Evaluation of the CO_2 sequestration capacity in Alberta's oil and gas reservoirs at depletion and the effect of underlying aquifers. *J. Can. Pet. Technol.* **2003**, *42*, 51−61.

(12) Hasanvand, M. z.; Ahmadi, M. A.; Shadizadeh, S. R.; Behbahani, R.; Feyzi, F. Geological storage of carbon dioxide by injection of carbonated water in an Iranian oil reservoir: A case study. *J. Pet. Sci. Eng.* **2013**, *111*, 170−177.

(13) Zhang, B.-b.; Song, X. Geological Storage of CO_2 to Enhance Coalbed Methane Production. *Adv. Mater. Res.* **2012**, *524−527*, 1173−1177.

(14) Zhang, L.; Li, X.; Zhang, Y.; Cui, G.; Tan, C.; Ren, S. CO_2 injection for geothermal development associated with EGR and geological storage in depleted high-temperature gas reservoirs. *Energy* **2017**, *123*, 139−148.

(15) Zhang, Y.; Oldenburg, C. M.; Finsterle, S.; Bodvarsson, G. S. System-level modeling for economic evaluation of geological CO_2 storage in gas reservoirs. *Energy Convers. Manage.* **2007**, *48*, 1827−1833.

(16) Arif, M.; Jones, F.; Barifcani, A.; Iglauer, S. Electrochemical investigation of the effect of temperature, salinity and salt type on brine/mineral interfacial propertiesMuhammad. *Int. J. Greenhouse Gas Control* **2017**, *59*, 136−147.

(17) Botto, J.; Fuchs, S. J.; Fouke, B. W.; Clarens, A. F.; Freiburg, J. T.; Berger, P. M.; Werth, C. J. Effects of Mineral Surface Properties on Supercritical CO_2 Wettability in a Siliciclastic Reservoir. *Energy Fuels* **2017**, *31*, 5275−5285.

(18) Iglauer, S. CO_2−Water−Rock Wettability: Variability, Influencing Factors, and Implications for CO_2 Geostorage. *Acc. Chem. Res.* **2017**, *50*, 1134−1142.

(19) Vilarrasa, V.; Carrera, J.; Olivella, S. Two-phase flow effects on the CO_2 injection pressure evolution and implications for the caprock geomechanical stability. In *3rd European Conference on Unsaturated Soils "E-UNSAT 2016"*; Delage, P., Cui, Y.-J., Ghabezloo, S., Pereira, J.-M., Tang, A.-M., Eds.; E3S Web of Conferences; EDP Sciences: Paris, 2016; Vol. 9, UNSP 04007.

(20) Kim, S.; Santamarina, J. C. CO_2 breakthrough and leak-sealing - Experiments on shale and cement. *Int. J. Greenhouse Gas Control* **2013**, *19*, 471−477.

(21) Zhang, S.; Diao, Y.; Cheng, X.; Zhang, X.; Zhang, Y.; Zheng, B.; Zhao, X. CO_2 Geological Storage Leakage Routes and Environment Monitoring. *J. Glaciol. Geocryol.* **2010**, *32*, 1251−1261.

(22) Chiquet, P.; Broseta, D.; Thibeau, S. Wettability alteration of caprock minerals by carbon dioxide. *Geofluids* **2007**, *7*, 112−122.

(23) D'Alessandro, D. M.; Smit, B.; Long, J. R. Carbon Dioxide Capture: Prospects for New Materials. *Angew. Chem., Int. Ed.* **2010**, *49*, 6058−6082.

(24) Khosharay, S.; Varaminian, F. Modeling interfacial tension of $(CH_4 + N_2) + H_2O$ and $(N_2 + CO_2) + H_2O$ systems using linear gradient theory. *Korean J. Chem. Eng.* **2013**, *30*, 724−732.

(25) Chow, Y. T. F.; Maitland, G. C.; Trusler, J. P. M. Interfacial tensions of the $(CO_2 + N_2 + H_2O)$ system at temperatures of (298 to 448) K and pressures up to 40 MPa. *J. Chem. Thermodyn.* **2016**, *93*, 392−403.

(26) Saraji, S.; Piri, M.; Goual, L. The effects of SO_2 contamination, brine salinity, pressure, and temperature on dynamic contact angles and interfacial tension of supercritical CO_2/brine/quartz systems. *Int. J. Greenhouse Gas Control* **2014**, *28*, 147−155.

(27) Chow, Y. T. F.; Eriksen, D. K.; Galindo, A.; Haslam, A. J.; Jackson, G.; Maitland, G. C.; Trusler, J. P. M. Interfacial tensions of systems comprising water, carbon dioxide and diluent gases at high

pressures: Experimental measurements and modelling with SAFT-VR Mie and square-gradient theory. *Fluid Phase Equilib.* **2016**, *407*, 159−176.

(28) Ren, Q. Y.; Chen, G. J.; Yan, W.; Guo, T. M. Interfacial tension of (CO_2 + CH_4) plus water from 298 to 373 K and pressures up to 30 MPa. *J. Chem. Eng. Data* **2000**, *45*, 610−612.

(29) Liu, Y. L.; Li, H. A.; Okuno, R. Measurements and Modeling of Interfacial Tension for CO_2/CH_4/Brine Systems under Reservoir Conditions. *Ind. Eng. Chem. Res.* **2016**, *55*, 12358−12375.

(30) Shah, V.; Broseta, D.; Mouronval, G.; Montel, F. Water/acid gas interfacial tensions and their impact on acid gas geological storage. *Int. J. Greenhouse Gas Control* **2008**, *2*, 594−604.

(31) Al-Yaseri, A.; Sarmadivaleh, M.; Saeedi, A.; Lebedev, M.; Barifcani, A.; Iglauer, S. N_2 + CO_2 + NaCl brine interfacial tensions and contact angles on quartz at CO_2 storage site conditions in the Gippsland basin, Victoria/Australia. *J. Pet. Sci. Eng.* **2015**, *129*, 58−62.

(32) Saghafi, A.; Javanmard, H.; Pinetown, K. Study of coal gas wettability for CO_2 storage and CH_4 recovery. *Geofluids* **2014**, *14*, 310−325.

(33) Bagherzadeh, S. A.; Englezos, P.; Alavi, S.; Ripmeester, J. A. Influence of Hydrated Silica Surfaces on Interfacial Water in the Presence of Clathrate Hydrate Forming Gases. *J. Phys. Chem. C* **2012**, *116*, 24907−24915.

(34) McCaughan, J.; Iglauer, S.; Bresme, F. Molecular dynamics simulation of water/CO_2-quartz interfacial properties: application to subsurface gas injection. *Energy Procedia* **2013**, *37*, 5387−5402.

(35) Chen, C.; Zhang, N.; Li, W.; Song, Y. Water Contact Angle Dependence with Hydroxyl Functional Groups on Silica Surfaces under CO_2 Sequestration Conditions. *Environ. Sci. Technol.* **2015**, *49*, 14680−14687.

(36) Vanommeslaeghe, K.; MacKerell, A. D. CHARMM additive and polarizable force fields for biophysics and computer-aided drug design. *Biochim. Biophys. Acta, Gen. Subj.* **2015**, *1850*, 861−871.

(37) Nieto-Draghi, C.; de Bruin, T.; Perez-Pellitero, J.; Bonet Avalos, J.; Mackie, A. D. Thermodynamic and transport properties of carbon dioxide from molecular simulation. *J. Chem. Phys.* **2007**, *126*, 064509.

(38) Martin, M. G.; Siepmann, J. I. Transferable potentials for phase equilibria. 1. United-atom description of n-alkanes. *J. Phys. Chem. B* **1998**, *102*, 2569−2577.

(39) Rahmatipour, H.; Azimian, A. R.; Atlaschian, O. Study of fluid flow behavior in smooth and rough nanochannels through oscillatory wall by molecular dynamics simulation. *Phys. A* **2017**, *465*, 159−174.

(40) Nath, S. K. Molecular simulation of vapor-liquid phase equilibria of hydrogen sulfide and its mixtures with alkanes. *J. Phys. Chem. B* **2003**, *107*, 9498−9504.

(41) Emami, F. S.; Puddu, V.; Berry, R. J.; Varshney, V.; Patwardhan, S. V.; Perry, C. C.; Heinz, H. Force Field and a Surface Model Database for Silica to Simulate Interfacial Properties in Atomic Resolution. *Chem. Mater.* **2014**, *26*, 2647−2658.

(42) Nath, S. K.; Escobedo, F. A.; de Pablo, J. J. On the simulation of vapor−liquid equilibria for alkanes. *J. Chem. Phys.* **1998**, *108*, 9905−9911.

(43) Phillips, J. C.; Braun, R.; Wang, W.; Gumbart, J.; Tajkhorshid, E.; Villa, E.; Chipot, C.; Skeel, R. D.; Kale, L.; Schulten, K. Scalable molecular dynamics with NAMD. *J. Comput. Chem.* **2005**, *26*, 1781−1802.

(44) Darden, T.; York, D.; Pedersen, L. Particle Mesh Ewald - an N.Log(N) Method for Ewald Sums in Large Systems. *J. Chem. Phys.* **1993**, *98*, 10089−10092.

(45) Tuckerman, M.; Berne, B. J.; Martyna, G. J. Reversible Multiple Time Scale Molecular-Dynamics. *J. Chem. Phys.* **1992**, *97*, 1990−2001.

(46) Martyna, G. J.; Tobias, D. J.; Klein, M. L. Constant-Pressure Molecular-Dynamics Algorithms. *J. Chem. Phys.* **1994**, *101*, 4177−4189.

(47) Humphrey, W.; Dalke, A.; Schulten, K. VMD: Visual molecular dynamics. *J. Mol. Graphics* **1996**, *14*, 33−38.

(48) Chen, C.; Chai, Z.; Shen, W.; Li, W.; Song, Y. Wettability of Supercritical CO2−Brine−Mineral: The Effects of Ion Type and Salinity. *Energy Fuels* **2017**, *31*, 7317−7324.

(49) Duan, Z. H.; Sun, R.; Liu, R.; Zhu, C. Accurate thermodynamic model for the calculation of H2S solubility in pure water and brines. *Energy Fuels* **2007**, *21*, 2056−2065.